

# Eliminating centre discrepancies between simultaneously captured ILIDS and PIV images by means of direct homography estimation

Sebastian Kosch and Nasser Ashgriz<sup>1, a)</sup>

*Department of Industrial and Mechanical Engineering, University of Toronto*

Interferometric Laser Imaging for Droplet Sizing (ILIDS a.k.a. MSI or IPI) requires the objective lens to be defocused so that fringe patterns can be imaged. When two cameras are used (e.g. to perform simultaneous PIV and ILIDS measurements or to assist in the detection of overlapping droplet images) this defocusing introduces a distortion that thwarts an accurate calibration of the two cameras and makes a successful registration of the two images impossible. To overcome the obvious difficulties presented by empirical ad-hoc estimates of this “centre discrepancy” distortion, we propose that existing feature-based registration and/or point set registration algorithms can be used on the images to find the correct homography directly. Our approach eliminates the need for camera calibration and leads to greatly improved matching between images.

## I. INTRODUCTION

Interferometric Laser Imaging for Droplet Sizing (ILIDS), also known as IPI (Interferometric Particle Imaging) and MSI (Mie Scattering Imaging) is an optical droplet sizing method. Its basic principle is based on the way a laser sheet is scattered by a spherical droplet: from a lateral perspective, the laser sheet is reflected and refracted into two glare points on the droplet sphere. When imaged through a lens away from the focal plane, the glare points—being sources of coherent monochromatic light—cast a circular fringe pattern, henceforth referred to as a disk. The spatial frequency of the fringes is (to a very close approximation) linearly related to the particle size. The phenomenon was first described by König, Anders, and Frohn<sup>1</sup> and later in greater detail by Glover, Skippon, and Boyle<sup>2</sup>.

The ability to image a whole 2D field of droplets all at once, ILIDS’ strongest selling point, is also its curse: when droplets are spaced too closely, their defocused disk images overlap and it becomes difficult to determine the fringe counts corresponding to individual droplets. Damaschke, Nobach, and Tropea<sup>3</sup> provide a statistical estimate on the fraction of overlapping disks (overlap coefficient).

Arguably the most popular way to reduce the amount of overlap is the use of optical compression techniques, whether by means of a slit aperture<sup>4</sup> or a cylindrical lens<sup>5,6</sup>. However, since some techniques (e.g. Global Phase-Doppler<sup>7</sup> and intensity-analyzing methods<sup>8</sup>) or situations (e.g. very low signal-to-noise ratios) rely on the full disk image being available, optical compression/integration is not always a feasible option. Therefore an alternative method of dealing with overlap exists: by identifying the contours of the overlapping disks, the fringe frequency analysis can be limited to the non-overlapping regions of each disk or can be modified to take the overlapping fringes into account.

## A. Calibration and centre discrepancies

Although a single camera is in theory sufficient to capture an ILIDS image, two cameras are often used in practice. One important reason is that a focused image, taken at the same instant as the defocused image, can provide a basis for the identification of overlapping disks mentioned above. This is the case, for instance, for the ILIDS system sold by Dantec Inc. Another reason for using two cameras can be the experimental requirement to perform two types of measurements simultaneously; examples of this are provided by Hardalupas, Sahu, and Taylor<sup>9</sup> (ILIDS and LIF) and Hardalupas *et al.*<sup>10</sup> (ILIDS and PIV).

To allow both cameras to image the same physical region in the spray, they are either placed behind a beam-splitter at a right angle to the light sheet, or placed separately at different angles. The latter approach makes for a more difficult setup, since Scheimpflug’s rule demands that the camera must be tilted with respect to the objective lens, but it gives the user the freedom to choose the highest-intensity scattering angle.

In any of the above cases, the use of two cameras requires that their images be mapped onto one another. This is commonly achieved by means of a camera calibration procedure, in which a target pattern (e.g. as in FIG. 1) of known dimensions is photographed by each camera. A pattern recognition algorithm then determines the object-to-image mappings for each camera:

$$\begin{bmatrix} x' \\ y' \\ z' \\ r' \end{bmatrix} = \begin{bmatrix} S_x & A_{yx} & A_{zx} & T_x \\ A_{xy} & S_y & A_{zy} & T_y \\ A_{xz} & A_{xy} & S_z & T_z \\ P_x & P_y & P_z & S_0 \end{bmatrix} \begin{bmatrix} x \\ y \\ z \\ 1 \end{bmatrix}. \quad (1)$$

In practice,  $P_{x,y,z} = 0$  and  $S_0 = 1$  is assumed, such that the mapping is affine. The  $z$ -components (third row/column) are further assumed to be zero, such that a  $3 \times 3$  matrix suffices for the purposes of this discussion:

$$\begin{bmatrix} x' \\ y' \\ r' \end{bmatrix} = \begin{bmatrix} S_x & A_{yx} & T_x \\ A_{xy} & S_y & T_y \\ P_x & P_y & S_0 \end{bmatrix} \begin{bmatrix} x \\ y \\ 1 \end{bmatrix}. \quad (2)$$

<sup>a)</sup> Electronic mail: {skosch,ashgriz}@mie.utoronto.ca

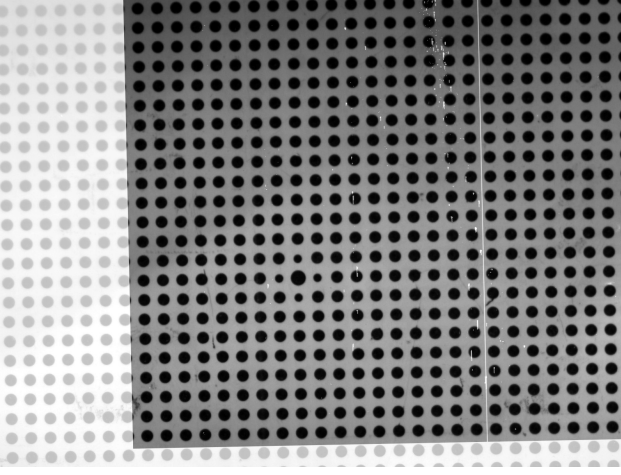


FIG. 1. Homography  $\mathbf{H}$  applied to target pattern image captured by the focused camera and superimposed on the image captured by the defocused camera (here, both cameras were in focus for the calibration only).

The calibration algorithm thus finds the camera matrices  $\mathbf{P}_{\text{foc}}$  and  $\mathbf{P}_{\text{def}}$  mapping the object coordinates  $\mathbf{x}$  onto the two camera images  $\mathbf{x}'_{\text{foc}}$  and  $\mathbf{x}'_{\text{def}}$  (the respective subscripts shall hence designate the focused and defocused cameras):

$$\mathbf{x}'_{\text{foc}} = \mathbf{P}_{\text{foc}} \mathbf{x} \quad (3)$$

$$\mathbf{x}'_{\text{def}} = \mathbf{P}_{\text{def}} \mathbf{x}. \quad (4)$$

It follows that the quotient of the two matrices, also known as the homography

$$\mathbf{H} = \mathbf{P}_{\text{def}} \mathbf{P}_{\text{foc}}^{-1} \quad (5)$$

can be used to map the focused image onto the defocused image, as shown in FIG. 1:

$$\mathbf{H} \mathbf{x}'_{\text{foc}} = \mathbf{x}'_{\text{def}}. \quad (6)$$

Unfortunately, the calibration procedure itself introduces an unwanted distortion: to capture a viable photo of the target pattern, the defocused camera must be temporarily brought into focus, as was done in FIG. 1. This is not mentioned e.g. in the application manual of Dantec's IPI system, but is a practical necessity. Bringing a camera out of focus not only introduces a blur, it also scales the image extents. FIG. 2, reproduced from Hardalupas *et al.*<sup>10</sup>, shows schematically how this effect creates “centre discrepancies”: since the extents of the defocused image are either smaller or larger than those of the focused image, depending on the direction of defocusing, all droplet images are projected either closer to or farther away from the image centre, and the discrepancy is worst for droplets far away from the image centre. As a result, the centres of objects in simultaneously captured focused and defocused images no longer align (FIG. 3); the calibration procedure is self-defeating.

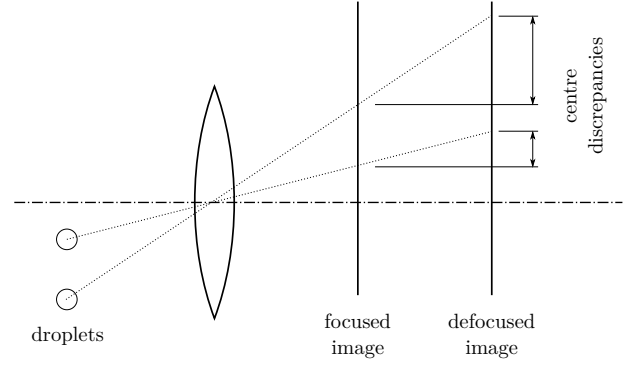


FIG. 2. Schematic showing the source of centre discrepancies in the case of parallel image and object planes

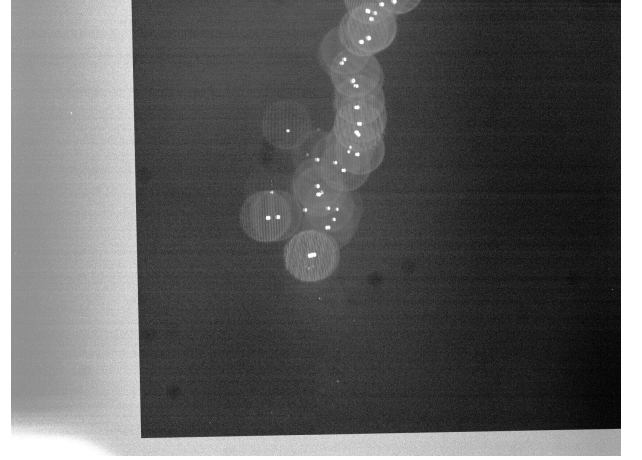


FIG. 3. Focused camera image, after applying homography  $\mathbf{H}$  derived from the calibration images, is superimposed onto defocused camera image of droplets. Discrepancies between object centres grow towards the edge of the image.

While this error is easy to account for in the ideal case of right angles and perfect alignments—simply rescaling the image would solve the problem—the situation becomes more difficult in practice when the target pattern is no longer parallel to the camera sensor (intentionally or accidentally) or when cylindrical lenses are used to add optical compression. In fact, there is no guarantee that affine mappings are sufficient in the general case.

## B. Context and structure of this paper

Surprisingly, only Hardalupas, Sahu, and Taylor<sup>9</sup> and Hardalupas *et al.*<sup>10</sup> have hitherto published a discussion of this effect, and the only previous mention known to the authors is in Kurosawa, Hishida, and Maeda<sup>11</sup>, who dismissed it as a “positioning error”.

Hardalupas *et al.* identified the centres of particles in both PIV (focused) and ILIDS (defocused) images. They then empirically estimated the magnitude of the centre discrepancy effect along the vertical axis, which enabled

them to improve the accuracy of their nearest-neighbour-based droplet image matching algorithm.

In this article, we show that existing algorithms developed by the computer vision community in recent years can obviate the need for calibration entirely. Instead, we can use visual correspondences between the focused and defocused images to find the mapping between them directly. To that end, we first provide in Section II a brief overview over popular methods in the field of automated (linear) *registration*, i.e. the art of finding a *homography* (geometric mapping) between two *epipolar images* (images of the same object, taken from different positions and angles). Section III documents our approach in greater detail and shows the result of a successful recalibration. While our goal was to automatically identify the disk centres in an uncompressed ILIDS image, a somewhat different approach is needed to automate the correction procedure proposed by Hardalupas *et al.*; we identify some relevant algorithms in Section IV.

## II. REVIEW OF IMAGE REGISTRATION TECHNIQUES

Given two identical images that have been rotated, shifted or even scaled with respect to one another, the applied transformation can theoretically be found by means of a brute-force search. This method is not feasible in practice, not only because of its enormous computational complexity (there are no gradients to guide the search) but also because of its inability to deal with noise, focal blur, perspective changes and other nonlinearities introduced by the photographic process. Conversely, normalized cross-correlation measures between images, as commonly used in PIV, are unaffected by noise but not invariant to rotation and scale and therefore not generally practicable. The standard approach to image registration is therefore a three-step process. First, *keypoints*, i.e. “interesting” points in the images are found by a keypoint detection algorithm. Then, a small image patch at every keypoint is extracted and converted into a *feature vector*, a set of numbers providing a very general description of the image patch that accounts for scale, rotation, blur, contrast, etc. Finally, matches between similar feature vectors from the two images are found, outliers are removed, and the homography is calculated.

However, the results of a keypoint detection algorithm must be as repeatable as possible, i.e. the same set of keypoints should be found in both images regardless of their relative position, rotation, scale, etc. For instance, the Harris corner detector<sup>12</sup>, one of the earliest keypoint detectors, is sensitive to scale and thus often unusable.

The recent decade has seen a rapidly growing collection of proposed keypoint detectors, beginning with SIFT<sup>13</sup>, SURF<sup>14</sup> and BRISK<sup>15</sup>, all of which include keypoint extractors, to CENSURE<sup>16</sup>, optimized for speed, and FAST<sup>17</sup>, which incorporates machine learning methods. Finally, the recent publication of ORB<sup>18</sup> includes a rotation-aware version of FAST used in this paper. Many more have been

developed but are not included here for brevity’s sake.

Keypoint extractors (sometimes called *descriptors*) are often optimized for and therefore included with keypoint detectors, as in the instances mentioned above. Some, however, are standalone algorithms such as BRIEF<sup>19</sup>.

It is straightforward to find matching keypoints by searching for pairs with the smallest arithmetic distance between their feature vectors (e.g. using the  $L^2$  norm). This nearest-neighbour search can be done exhaustively in linear time to find the optimal matching, but many faster, if approximate, search methods exist. We should note FLANN<sup>20</sup>, a publicly available collection of such implementations which includes a fully automatic parameter selection heuristic.

Finally, the homography—assuming one exists—can be derived from the set of matched keypoint coordinate pairs. Since many of the found matches will be wrong, it is of essence to use a robust estimator, i.e. a type of regression model designed to ignore outliers. Possibly the oldest of these methods is RANSAC<sup>21</sup>, an iterative procedure in which sets of data points are chosen at random and discarded if the agreement between a model fit to them and all other data points falls below a carefully chosen threshold. RANSAC was used for this paper, although other robust methods exist. The criterion developed by Moisan and Stival<sup>22</sup> deserves special mention in our context; it does away with RANSAC’s hard threshold and instead takes into consideration the probability of a match to be in consensus with epipolar geometry.

## III. USING AFFINE ORIENTED FAST, BRIEF AND RANSAC TO ESTIMATE THE HOMOGRAPHY BETWEEN PIV AND ILIDS PHOTOGRAPHS

Existing PIV/ILIDS systems derive the homography from the result of a camera calibration procedure which the user is required to perform before analyzing images. Although the final value of  $\mathbf{H}$  is invisible to the user in our copy of Dantec’s DynamicStudio software, the camera matrices  $\mathbf{P}_{\text{foc}}$  and  $\mathbf{P}_{\text{def}}$  can be shown and edited. We therefore must find a corrected homography  $\hat{\mathbf{H}}$  that allows us to compute

$$\hat{\mathbf{P}}_{\text{def}} = \hat{\mathbf{H}} \mathbf{P}_{\text{foc}} \quad (7)$$

so that we can replace  $\mathbf{P}_{\text{def}}$  with  $\hat{\mathbf{P}}_{\text{def}}$  in the software, effectively correcting  $\mathbf{H}$  to  $\hat{\mathbf{H}}$ .

To efficiently extract keypoints, we combined three algorithms: ASIFT<sup>23</sup> to deal with skew transformations; an oriented version of FAST, published as part of ORB, to detect keypoints; and standard BRIEF as a keypoint extractor.

ASIFT is a method originally developed to be used with SIFT. It introduces invariance to affine mappings by simulating various projective transformations while FAST and BRIEF are run repeatedly. Unsurprisingly, this slows the analysis down, but given the infinitude of possible an-



FIG. 4. Simulating disks based on the focused image.

gled camera-camera-object configurations, it is wise to maintain a flexible framework.

We should note that the original ASIFT with SIFT works well, but SIFT is encumbered by patents. To encourage vendors of imaging systems to adopt the proposed algorithms, we made it our goal to find a freely available replacement.

Recall that the disks in the defocused image are missing from the focused image, rendering a registration between them impossible. It is straightforward to simulate the disks, however. We followed the following protocol on our focused images:

1. Mask the image, blacking out all areas that are known not to contain droplets.
2. Subtract the pixel-wise minimum or mean value taken over all images taken by the camera. This step serves to black out defective hot pixels on the camera's CCD and other static noise.
3. Erode the image, using a  $3 \times 3$  or  $5 \times 5$  kernel. This will close any remaining bright pixels which are likely noise.
4. Locate the intensity peaks in the remaining image.
5. Fill a blank image with black, then draw bright circles of diameter  $D_{\text{disk}}$  onto it, centred at the respective positions of the intensity peaks detected in the focused image. (Note that simply dilating the result of the previous step will not lead to circular disks.)

The result of performing these operations on our sample image is shown in FIG. 4. We determined the disk diameter  $D_{\text{disk}}$  empirically from the defocused images, although it is naturally preferable to automate this step, e.g. using circular Hough transforms or cross-correlation with circular masks. There may be simpler ways of achieving the same result, e.g. by means of Gaussian filters, distance transforms and thresholding operations. However, we found the protocol described above to be quite robust to noise and fast enough for our application.

Implementations of ORB and BRIEF are freely available through the OpenCV project, which provides bindings for the C++ and Python languages. We used these implementations to find and extract matching keypoints between our sample images, shown in FIG. 5.

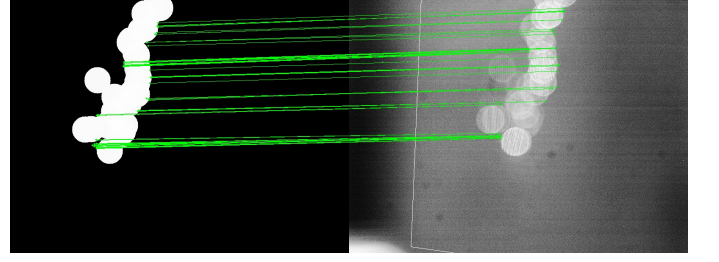


FIG. 5. Visualized inliers in the set of matched keypoints between the mirrored simulated disks (see FIG. 4) and the ILIDS image.

The matches shown in FIG. 5 were found using a most basic method: brute-force match search, followed by a RANSAC estimation of the homography matrix  $\mathbf{K}$  using a threshold of 10.

Since the two cameras were positioned behind a beam-splitter in our setup, the defocused image was flipped horizontally. We therefore first mirrored it horizontally, using the transformation matrix

$$\mathbf{M}_h = \begin{bmatrix} -1 & 0 & (\text{image width}) \\ 0 & 1 & 0 \\ 0 & 0 & 1 \end{bmatrix}.$$

To speed up the image registration process, it can be helpful to first down-scale the images. To reduce an image to half of its original size, apply

$$\mathbf{S}_{0.5} = \begin{bmatrix} 0.5 & 0 & 0 \\ 0 & 0.5 & 0 \\ 0 & 0 & 1 \end{bmatrix}.$$

While the above operations might not be strictly necessary, we found that they significantly improved the quality of the matches identified. If the registration algorithms mentioned above now find a homography matrix  $\mathbf{K}$ , then we can write

$$\mathbf{K} \mathbf{M}_h \mathbf{S}_{0.5} \mathbf{P}_{\text{foc}} = \mathbf{S}_{0.5} \mathbf{P}_{\text{def}} \quad (8)$$

and to bring this into a form similar to (6),

$$\mathbf{S}_{0.5}^{-1} \mathbf{K} \mathbf{M}_h \mathbf{S}_{0.5} \mathbf{P}_{\text{foc}} = \mathbf{S}_{0.5}^{-1} \mathbf{S}_{0.5} \mathbf{P}_{\text{def}} \quad (9)$$

$$= \mathbf{P}_{\text{def}} \quad (10)$$

Finally, it turns out that Dantec's DynamicStudio software violates convention by placing the coordinate origin at the bottom (not top) left corner of the image. We must therefore pre- and post-multiply by  $\mathbf{M}_v^{\pm 1}$ , with

$$\mathbf{M}_v = \begin{bmatrix} 1 & 0 & 0 \\ 0 & -1 & (\text{image height}) \\ 0 & 0 & 1 \end{bmatrix},$$

to arrive at our final expression for  $\hat{\mathbf{H}}$ :

$$\hat{\mathbf{H}} = \mathbf{M}_v \mathbf{S}_{0.5}^{-1} \mathbf{K} \mathbf{M}_h \mathbf{S}_{0.5} \mathbf{M}_v^{-1}. \quad (11)$$

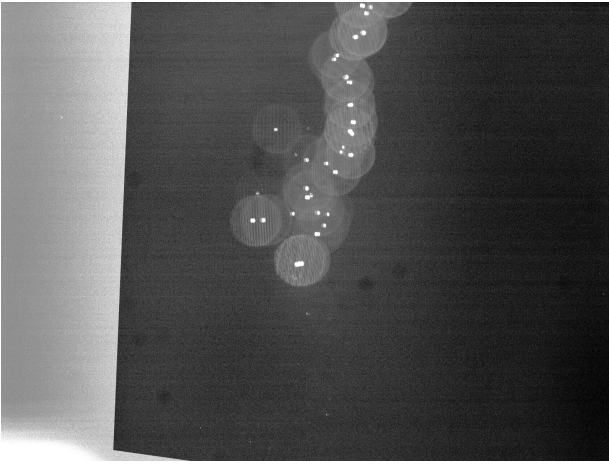


FIG. 6. Focused camera image, after applying corrected homography  $\hat{\mathbf{H}}$  derived from the matched keypoints, is superimposed onto defocused camera image of droplets.

Substitution of  $\hat{\mathbf{H}}$  into (7) yields  $\hat{\mathbf{P}}_{\text{def}}$ , which can be manually entered into the DynamicStudio software. FIG. 6 illustrates how the use of  $\hat{\mathbf{H}}$  leads to an improved alignment compared to FIG. 3. Note that a slight projective distortion is necessary for optimal registration, confirming that it is infeasible to restrict the homography to affine matrices.

#### IV. POINT SET REGISTRATION BETWEEN DROPLET CENTRES FROM TWO IMAGES

The keypoint matching approach used in the previous section relies on feature information extracted from the disk images, but those are not available when a slit aperture is installed to reduce overlap. While slit strip images could be simulated over the focused image (in a procedure analogous to that illustrated in FIG. 4), the lack of overlap between them could make it significantly more difficult to find “interesting” keypoints in the simulated image. Keypoints are not required, however, when the absence of overlap allows us to identify focused and defocused object centres directly and find a projection mapping between them.

Indeed, Hardalupas *et al.* successfully registered their PIV and ILIDS images that way: using wavelet transforms at various frequencies, they identified the putative droplet centres on both focused and defocused images. Then, using a continuous, single-stream monodisperse droplet generator, they estimated how the magnitude of the centre discrepancies varies over the image. After applying this empirically estimated distortion to the captured images, they matched each focused droplet to the closest defocused droplet (if one can be found within an subjectively chosen search distance).

Although they reported good success using this method, it requires both an empirical estimation of the

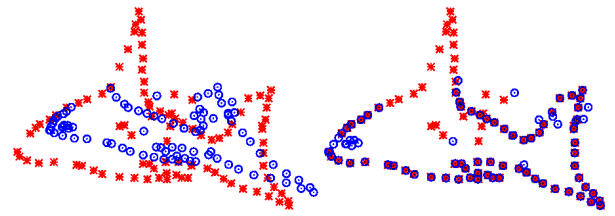


FIG. 7. Non-rigid variant of the Coherent Point Drift algorithm applied to two point sets. Notice that the probabilistic nature of the matching creates robustness to unmatched points. (Image source: Wikipedia)

centre discrepancies every time the camera is defocused *and* a guess at the appropriate search window size. Moreover, mismatches are likely as the naive closest-neighbour search is not robust to noise. To eliminate these steps, we suggest that droplet matches be found directly using a robust point set registration algorithm.

Since the early 1990s, computer vision researchers have accumulated an impressive body of work on this topic, most of it focusing either on rigid transformations (i.e. translation and rotation only) or non-rigid transformations (typically understood to include nonlinear warping). The problem at hand requires an algorithm able to deal with projective transforms, which are non-rigid but linear.

The only paper known to the authors to specifically address this case is by Chi, Ho, and Yang<sup>24</sup>, who propose an iterative search based on image moments. Since image moments are an aggregate metric, they do not directly lead to a droplet-to-droplet correspondence. Still, closest-neighbour matches after application of this algorithm would likely produce results no worse than those found after estimating the transformation empirically.

Robust non-rigid methods are also applicable in this case and deserve some mention. Many of them are probabilistic relaxations of the Iterative Closest Point algorithm, which simply searches for the least-squares-optimal rigid mapping. Several of these approaches were reviewed and generalized by Jian and Vemuri<sup>25</sup>. A slightly different approach, named Coherent Point Drift<sup>26</sup>, is also highly popular and illustrated in FIG. 7.

We forgo at this point a documentation of the application and refer the reader to Hardalupas *et al.*, who describe their centre identification technique in good detail, and to the above-mentioned authors, who have published freely available implementations of their algorithms online.

#### V. CONCLUSION

Existing image registration algorithms, developed primarily for applications in robotics and medical imaging, can eliminate the need for camera calibration and sidestep the centre discrepancy effect in simultaneous fo-

cused/defocused imaging configurations. We have shown how feature-based registration algorithms can be used to estimate homographies between PIV and ILIDS disk images, and we have suggested several point set registration methods that will align images based purely on object centre positions.

In the short term, increased awareness about the centre discrepancy effect and its origin should help assure ILIDS users that the “positioning error” is not a symptom of poor experimental setup but an easily explained optical effect. Ultimately, our hope is that by incorporating the reviewed algorithms in their software, commercial vendors of ILIDS systems will eliminate the need for calibration procedures altogether while improving the number of validated droplet matches.

- <sup>1</sup>G. König, K. Anders, and A. Frohn, *Journal of Aerosol Science* **17**, 157 (1986).
- <sup>2</sup>A. R. Glover, S. M. Skippon, and R. D. Boyle, *Applied Optics* **34**, 8409 (1995).
- <sup>3</sup>N. Damaschke, H. Nobach, and C. Tropea, *Experiments in Fluids* **32**, 143 (2002).
- <sup>4</sup>G. Pan, J. Shakal, W. Lai, R. Calabria, P. Massoli, and O. Pust, *Spray '06 – Workshop über Sprays, Erfassung von Sprühvorgängen und Techniken der Fluidzerstäubung* (2006).
- <sup>5</sup>T. Kawaguchi, Y. Akasaka, and M. Maeda, *Meas Sci Technol* **13**, 308 (2002).
- <sup>6</sup>M. Maeda, Y. Akasaka, and T. Kawaguchi, *Experiments in Fluids* **33**, 125 (2002).
- <sup>7</sup>N. Damaschke, S. Rasmussen, C. Tropea, and A. Woite, in *6th International Congress on Optical Particle Characterisation, Brighton, UK* (2001).
- <sup>8</sup>A. Quérel, P. Lemaître, M. Brunel, E. Porcheron, and G. Gréhan, in *15th International Symposium on Applications of Laser Techniques to Fluid Mechanics* (2010).
- <sup>9</sup>Y. Hardalupas, S. Sahu, and A. M. K. P. Taylor, in *15th International Symposium on Applications of Laser Techniques to Fluid Mechanics* (2010).
- <sup>10</sup>Y. Hardalupas, S. Sahu, A. M. K. P. Taylor, and K. Zarogoulidis, *Experiments in Fluids* **49**, 417 (2010).
- <sup>11</sup>R. Kurosawa, K. Hishida, and M. Maeda, in *11th International Symposium on Applications of Laser Techniques to Fluid Mechanics, Lisbon, Portugal* (2002).
- <sup>12</sup>C. Harris and M. Stephens, in *Proceedings of the Alvey Vision Conference 1988* (1988) pp. 23.1–23.6.
- <sup>13</sup>D. G. Lowe, in *International Journal of Computer Vision*, Vol. 60 (2004) p. 91.
- <sup>14</sup>H. Bay, A. Ess, T. Tuytelaars, and L. V. Gool, *Computer Vision and Image Understanding* **110**, 346 (2008).
- <sup>15</sup>S. Leutenegger, M. Chli, and R. Y. Siegwart, in *2011 IEEE International Conference on Computer Vision (ICCV)* (2011) pp. 2548–2555.
- <sup>16</sup>M. Agrawal, K. Konolige, and M. R. Blas, in *10th European Conference on Computer Vision* (2008) pp. 102–115.
- <sup>17</sup>E. Rosten and T. Drummond, in *2005 IEEE International Conference on Computer Vision (ICCV)*, Vol. 2 (2005) pp. 1508–1515.
- <sup>18</sup>E. Rublee, V. Rabaud, K. Konolige, and G. Bradski, in *2011 IEEE International Conference on Computer Vision (ICCV)* (2011) pp. 2564–2571.
- <sup>19</sup>M. Calonder, V. Lepetit, C. Strecha, and P. Fua, in *11th European Conference on Computer Vision*, Vol. LNCS 6314 (2010) pp. 778–792.
- <sup>20</sup>M. Muja and D. G. Lowe, in *International Conference on Computer Vision Theory and Applications* (2009) pp. 331–340.
- <sup>21</sup>M. A. Fischler and R. C. Bolles, *Communications of the ACM* **24**, 381 (1981).
- <sup>22</sup>L. Moisan and B. Stival, *International Journal of Computer Vision* **57**, 201 (2004).
- <sup>23</sup>J.-M. Morel and G. Yu, *SIAM Journal on Imaging Sciences* **2**, 438 (2009).
- <sup>24</sup>Y.-T. Chi, J. Ho, and M.-H. Yang, in *10th Asian Conference on Computer Vision* (2011) pp. 268–281.
- <sup>25</sup>B. Jian and B. C. Vemuri, *IEEE transactions on pattern analysis and machine intelligence* (2010).
- <sup>26</sup>A. Myronenko and X. Song, *IEEE transactions on pattern analysis and machine intelligence* **32**, 2262 (2010).